Check for updates

Research Article

INTERNATIONAL JOURNAL OF ADVANCED ROBOTIC SYSTEMS

International Journal of Advanced Robotic Systems
May-June 2019: 1–11
© The Author(s) 2019
DOI: 10.1177/1729881419847926
journals.sagepub.com/home/arx
SAGE

Application-oriented type synthesis and coupling kinematics analysis of a $1R^x2T^{yz}$ parallel stabilized platform for tunnel detection system

Xiao Liu[1], Bo Liu[1], Yingjie Duan[1] and Hui Bian[2]

Abstract

For collecting image high precisely, the application-oriented type synthesis and kinematics analysis for parallel vehicle-based stabilized platform are systematically carried out. Firstly, taking multi-camera install center and vehicle trajectory offset as research objects, the influence of external perturbation on visual system is analyzed quantitatively by numerical calculation and field testing. On this basis, a new type of 2SPR/RPS parallel mechanism with two-translational and one-rotational degree of freedoms is presented. Secondly, by analyzing the motion characteristic of 2SPR/RPS parallel mechanism, the motion adjoint transformation and input–output mapping for parallel vehicle-based stabilized platform are proposed by screw description of rigid-body movement. In addition, an experimental prototype is developed, and the results between numerical examples and semi-physical simulations are compared in order to prove the validity of theoretical analysis. Finally, based on the concept of influence of external perturbations on tunnel detecting system, an external parameter identify method for coupling pose and object distance of visual system is studied. The results can be extended to development, application, and performance evaluation for parallel vehicle-based stabilized platform in next step.

Keywords

Parallel mechanism, stabilized platform, type synthesis, kinematics analysis, visual detection

Date received: 17 December 2018; accepted: 29 March 2019

Topic: Robot Manipulation and Control
Topic Editor: Andrey V Savkin
Associate Editor: Istvan Harmati

Introduction

The traditional tunnel detection methods are generally implemented with artificial instruments on the premise of closing roads, which have many deficiencies such as (i) low work efficiency, (ii) high risk, and (iii) low detection precision.[1,2] Based on the advantages of high speed, low undetected rate, high precision, and easy to realize data management, the rapid detection method has become a research focus in transportation equipment development.[3–6] In recent years, researchers have begun to study intelligent detection method for expressway tunnel based on computer-vision technology.[7,8] Our development team

[1] Shanxi Engineering Research Center for Road Intelligent Monitoring, Shanxi Transportation Research Institute, Taiyuan, China
[2] Parallel Robot and Mechatronic System Laboratory of Hebei Province, Yanshan University, Qinhuangdao, China

Corresponding author:
Xiao Liu, Shanxi Engineering Research Center for Road Intelligent Monitoring, Shanxi Transportation Research Institute, Taiyuan, Shanxi 030006, China.
Email: liuxiao@ysu.edu.cn

Creative Commons CC BY: This article is distributed under the terms of the Creative Commons Attribution 4.0 License (http://www.creativecommons.org/licenses/by/4.0/) which permits any use, reproduction and distribution of the work without further permission provided the original work is attributed as specified on the SAGE and Open Access pages (https://us.sagepub.com/en-us/nam/open-access-at-sage).



Figure 1. The tunnel intelligent detection system.

developed a set of tunnel intelligent detection system which can complete detecting tunnel disease at a speed of 80 km/h, as shown in Figure 1.[9] However, due to the complex working environment of expressway tunnels, the tunnel intelligent detection system still have imperative problems such as narrow application range, weak anti-disturbance capability, and low-quality image.

Visual system is the core of the tunnel intelligent detection system that is composed by digital camera, laser light source, inertial navigation system, and mechanical device.[10] The perimeter of expressway tunnel section is about 20 m, but the geometrical dimensions of cracks and other diseases are small, generally 0.1–0.8 mm. For this reason, high-quality image acquisition is the precondition to process and identify tunnel disease.[11–13] However, due to external perturbations such as driver's subjective consciousness, traffic flow, and road bump, the posture between vehicle-based equipment and tunnel lining will be changed. In particular, the structure parameters of tunnels with different design speed are also various, which seriously affect image acquisition and lead to image blurry or unavailable to image.[14,15] Note that the digital camera of the tunnel detection system has a small depth of field (−200 to +200 mm) and rapidity driving speed (50–80 km/h); it is impossible to isolate the influence of external perturbations on visual acquisition system only by adjusting camera parameters in real time.[16] Therefore, a servo compensation mechanism is needed to realize the relative posture between digital cameras and tunnel lining surface keeping fixed.

The role of stabilized platform is to isolate external perturbations through a set of real-time compensation mechanism and provide a relatively stable environment for devices on plane, ship, and vehicle.[17,18] However, most of the existing stabilized platforms are two-axis or three-axis serial mechanisms, which are mainly used for attitude stability. Parallel mechanisms (PMs) are easy to realize spatial multi-axis compensation, which have advantages such as multi-degree of freedom (DOF) output and large movement range compared to serial mechanisms.[19,20] It is an ideal mechanism model for developing vehicle-based stabilized platform of tunnel visual detection. At present, the configuration of parallel stabilized platforms is mostly Stewart PMs, which need large space occupation and high energy consumption.[21,22] Therefore, it cannot be used in tunnel detection system.

On the other hand, parallel vehicle-based stabilized platform is a multi-rigid-body system in non-inertial frame. Nevertheless, the existing kinematics methods of PMs were analyzed in inertial frame.[23–25] Traditionally, kinematics relationship between inertial frame and non-inertial frame should be analyzed when investigating rigid-body problems in non-inertial frame.[26,27] Because the traditional description of rigid-body kinematics is described in terms of angular movement and linear movement of a point attached to it, it is more complicate and difficult to obtain a uniform mathematic model when analyzing a multi-rigid-body system, which makes it impossible to research the effects of vehicle perturbation on the performance of PMs.[28,29]

A review of the previous works reveals that modern mathematic tools, such as geometric algebra, spatial operator algebra, Grassmann–Cayley algebra, screw algebra, and Lie groups and Lie algebras, have been introduced to rigid-body kinematics analysis. Therefore, compared with other modern mathematical tool, screw theory and Lie groups and Lie algebras were more effective when the number of robot DOFs increases.[30] The pioneering treatise by Hunt laid the foundations for the screw theory,[31] and Duffy and Phillips promoted modern applications of the screw theory.[32,33] With these studies, the elaborate surveys have been contributed to the robot kinematics.[34,35]

Focusing on the above, this article is arranged as follows. Second section analyzes the influence of tunnel structure and external perturbation on visual system by numerical calculation and field testing and presents a new type of 2SPR/RPS PM with two-translational and one-rotational DOFs. In third section, based on motion characteristic analysis of 2SPR/RPS PM, the motion adjoint transformation and input–output mapping of parallel vehicle-based stabilized platform are proposed by screw description of rigid-body movement. Furthermore, numerical examples and semi-physical simulations included in fourth section that are performed to validate the mathematical models are presented in this article. Fifth section proposes an external parameter identifies and analysis method for coupling poses and object distance of visual system. Finally, the last section presents conclusions and future works.

Application-oriented type synthesis of parallel vehicle-based stabilized platform

The influence of tunnel structure parameters on visual system

The tunnel image acquisition system is composed of 6 digital cameras and 12 laser lights. The digital camera has parameters of diffusion angle 25°, depth of field 1.5–2.0 m, line frequency 45 kHz, and object distance 3.0 m. A sketch of cross-sectional outline of expressway tunnel is shown

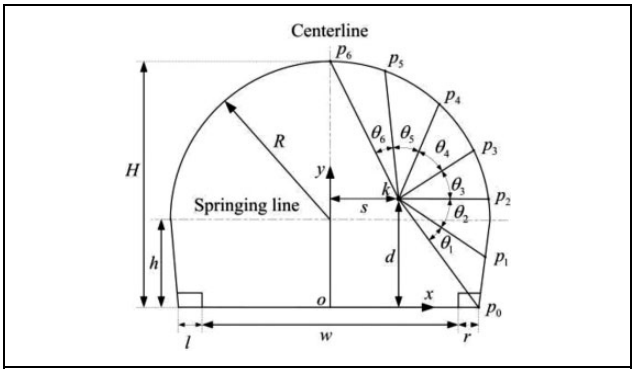


Figure 2. The cross-sectional outline of road tunnel.

in Figure 2, in which H denotes tunnel height, h denotes springing line height, R denotes springing line radius, w denotes lane width, and l and r denote width of left and right removal access, respectively.[36] The frame $\{o\}$ presents the center line of pavement, x-axis points to tunnel surface, and y-axis is vertical up. For the purpose of collecting image uniformly and completely, the half-range tunnel surface is divided into six parts. The relationship between above segmentation points is shown as follows

$$|\boldsymbol{p}_i - \boldsymbol{p}_{i-1}| = S/6 \tag{1}$$

where

$$S = \begin{cases} \pi R/2 + \sqrt{(R - l - w/2)^2 + h^2} & \text{left} - \text{range of tunnel} \\ \pi R/2 + \sqrt{(R - r - w/2)^2 + h^2} & \text{right} - \text{range of tunnel} \end{cases}$$

and $p_i (i = 0 \cdots 6)$ are the segmentation points of the half-range tunnel surface.

Let $\boldsymbol{k} = [\,s \quad d\,]^T$ denote the intersection point of multi-camera visual axes, and the range and working distance of each camera is given by

$$\begin{cases} \theta_i(s,d) = \cos^{-1}\left(\dfrac{(\boldsymbol{k} - \boldsymbol{p}_{i-1}) \cdot (\boldsymbol{k} - \boldsymbol{p}_i)}{|\boldsymbol{k} - \boldsymbol{p}_{i-1}| \times |\boldsymbol{k} - \boldsymbol{p}_i|}\right) \\ l_i(s,d) = (|\boldsymbol{k} - \boldsymbol{p}_i| + |\boldsymbol{k} - \boldsymbol{p}_{i-1}|)/2 \end{cases} \tag{2}$$

To ensure the accuracy of image collecting, the range and working distance of each camera should be kept consistent. Meanwhile, the range of camera should be as small as possible. For this reason, a mathematical description of multi-camera install center optimum can be given as

$$\begin{cases} find \;\; s, d \in R \\ min \;\; \boldsymbol{f}(s,d) = [\,\sigma_\theta(s,d) \quad \sigma_l(s,d) \quad max(\theta(s,d))\,]^T \\ s.t \quad s_{min} \le s \le s_{max}, d_{min} \le d \le d_{max} \end{cases} \tag{3}$$

where $\sigma_\theta(s,d)$ and $\sigma_l(s,d)$ are mean square of range and working distance of camera, respectively; $\boldsymbol{\theta}(s,d) = [\,\theta_1(s,d) \quad \ldots \quad \theta_6(s,d)\,]^T$ is the range vector of camera; $s_{\max}$, $s_{\min}$, $d_{\max}$, $d_{\min}$ are the upper and lower limits of variables s and d, respectively.

From equation (3), the objective function is composed by three single-object functions: (i) $f_1(s,d) = \sigma_\theta(s,d)$, (ii) $f_2(s,d) = \sigma_l(s,d)$, and (iii) $f_3(s,d) = \max(\theta(s,d))$. Within the range of variable d, the minimum of one single-object function is $f_i(s_0, d_i^*)$; in addition, the values of other single-object functions are $f_j(s_0, d_i^*)$, in which $j = 1, 2, 3$ and $j \neq i$. Then the minimum and maximum of each single-object function can be obtained as $f_i^{\min}(s_0)$ and $f_i^{\max}(s_0)$. On this basis, the membership function of variable d can be constructed as

$$u_i(s_0,d) = \begin{cases} 1 & f_i(s_0,d) \le f_i^{\min}(s_0) \\ \left(\dfrac{f_i^{\max}(s_0) - f_i(s_0,d)}{f_i^{\max}(s_0) - f_i^{\min}(s_0)}\right)^2 & f_i^{\min}(s_0) \le f_i(s_0,d) \le f_i^{\max}(s_0) \\ 0 & f_i(s_0,d) \ge f_i^{\max}(s_0) \end{cases} \tag{4}$$

In view of equation (4), the membership degree $u_i(s_0,d) \in [0,1]$ indicates the closeness of design variable d to optimal value. Taking maximum membership degree as optimization goal, the optimization model depended on variable d can be built as

$$\max \; u(s_0) = a_1 u_1(s_0,d) + a_2 u_2(s_0,d) + a_3 u_3(s_0,d) \tag{5}$$

where $a_i = (1 - u_i(s_0,d)) \Big/ (3 - \sum_{i=1}^{3} u_i(s_0,d))$ is the weight coefficient of each single-object function.

Substituting equations (3) and (4) into equation (5), the optimal value of multi-camera install center can be obtained as (s_0, d^*) when the variable s is s_0. Similarly, the corresponding optimal value can be obtained when the variable s takes different values. The parameter (s^*, d^*) whose membership degree is the largest can be regarded as an optimal result.

On this basis, the acquisition range of each camera should be the same to ensure image acquisition quality. Hence, the angle between assembly platform and x-axis of frame $\{o\}$ can be written as

$$\theta(s^*, d^*) = \cos^{-1} \boldsymbol{I}(\boldsymbol{k} - \boldsymbol{p}_3)/|\boldsymbol{k} - \boldsymbol{p}_3| \tag{6}$$

where $\boldsymbol{I} = (\,1 \quad 0\,)$.

Numerical calculation

Suppose the designed speed of expressway tunnel is 120 km/h, the structure parameters are $H = 8.12$ m, $h = 2.0$ m, $R = 6.12$ m, $w = 7.5$ m, $l = 0.75$ m, and $r = 1.25$ m.[36] According to the lane width, height limitation, and weight limitation of vehicle, the upper and lower bound of

Table 1. The optimal results of multi-camera install center when s is 1.9 m.

	$f_1(1.9, d_1^*)$	$f_2(1.9, d_2^*)$	$f_3(1.9, d_3^*)$	Optimal results
Object 1	2.75	2.84	3.62	2.88
Object 2	0.44	0.45	0.74	0.51
Object 3	28.15	28.65	26.70	27.23
Design variable	3.00	3.20	2.00	2.60

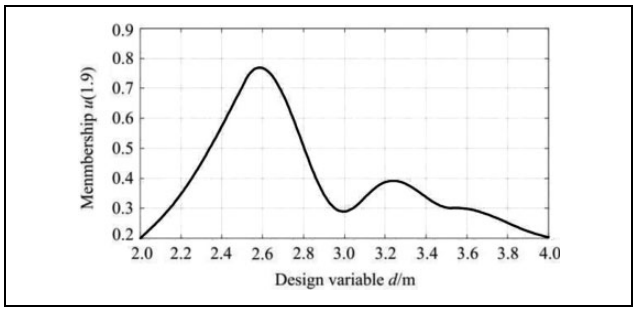


Figure 3. The change curves of membership when s is 1.9 m.

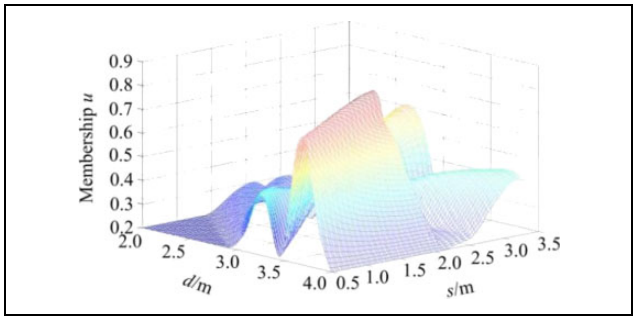


Figure 4. The change surface of global membership.

variable s and d can be formulated as 0.5 m, 3.5 m and 2.0 m, 4.0 m, respectively.

Suppose $s = 1.9$ m, the optimal result of single objective function within the scope of variable d can be calculated, as shown in Table 1. The minimum value of various single objective function is $f_1(1.9, 3.0) = 2.75$, $f_2(1.9, 3.2) = 0.45$, and $f_3(1.9, 2.0) = 26.7$, and the maximum and minimum values of various single objective function are (3.62, 3.62), (0.74, 0.42), and (28.65, 26.70), respectively. According to equations (4) and (5), when s is 1.9 m, a sketch of membership ($u(1.9)$) with design variable d is shown in Figure 3. It can be observed that the maximum value of membership is 0.77 when the design variable d is 2.6 m.

In a similar way, the membership $u(s)$ can be obtained by setting different value s within its scope (0.5–3.5 m). A sketch of global membership surface is shown in Figure 4. It can be seen that the maximum value of membership is 0.85 when the design variable values are $s = 2.0$ m and $d = 3.5$ m. In addition, by analyzing surface properties, the design variable d has much bigger effect on membership, but the design variable s, much smaller. On this basis, the angle between assembly platform and x-axis of frame $\{o\}$ can be obtained as 35.0° by equation (6).

Table 2. The optimal results of multi-camera install center in different working conditions

Working condition (km/h)	Calculation result
60	(1.7 m, 2.4 m, 25.1°)
80	(1.9 m, 2.8 m, 28.7°)
100	(1.9 m, 3.0 m, 32.9°)
120	(2.0 m, 3.5 m, 35.0°)

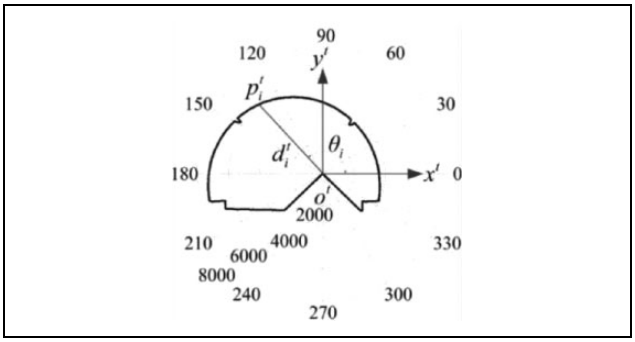


Figure 5. The vehicle trajectory at time t.

Similarly, suppose the designed speed of expressway tunnel is 60, 80, and 100 km/h, respectively. The install center parameter of visual system and angle of assembly platform are calculated separately, as shown in Table 2. The variation range of multi-camera install center in different working conditions is Tx: ± 0.15 m, Ty: ± 0.55 m, and Rz: $\pm 0.5°$.

The influence of vehicle perturbation posture on visual system

Let $o^t - x^t y^t z^t$ denote reference frame attached to laser three-dimensional (3-D) scanner, the origin established at the center of laser 3-D scanner, x^t-axis is perpendicular to tunnel surface, y^t-axis is vertical up, and z^t-axis points to the direction of vehicle running, as shown in Figure 5. Beyond that, $p_i^t (i = 1, 2, \cdots, 1080)$ denotes the points on tunnel surface; θ_i denotes the angle between corresponding laser beam of point p_i^t and x^t-axis; d_i^t denotes the distance of point p_i^t to the origin of frame $\{o^t\}$. The expression of vehicle trajectory offset at time t is given as $\xi^t = \sum_{i=1}^{n} (d_i^t \cos\theta_i) \Big/ n$.

In order to obtain experimental data, the field tests are carried out in Zijinshan tunnel of Pingyu highway (4511 m), Hongtiguan tunnel of Changping highway (13,098 m), Hejiabao tunnel of Baomao highway (2004 m), and Luoping tunnel of Fenwu highway (4596 m), respectively. Due to the limitation of space, the experimental data of vehicle

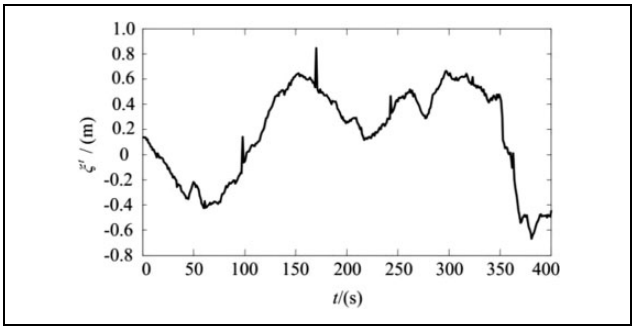


Figure 6. The vehicle trajectory offset.

trajectory offset in Zijinshan tunnel are introduced, as shown in Figure 6. It can be seen that the variation range of vehicle trajectory offset is Tx: −0.6 to 0.6 m.

Type synthesis of $1R^x2T^{yz}$ PM

According to the analysis performed in the previous section, a type of $1R^x2T^{yz}$ PMs should be synthesized to compensate the effect of external perturbation. According to the PM theory, the constraint screw system of actuated branch has three situations. The constraint screw system should be as less as possible to ensure rotation axis continuous in vehicle-based stabilized platform. Hence, the PMs which have one constraint force and five actuated branches should be synthesized in this article. Based on the concept of mathematics criterion of rigid-body continuous rotation axis,[37] the constraint screw should actually be parallel to each other but not coplanar.

The typical structural form of five-DOF actuated branch is RPS or SPR. For RPS actuated branch, the constraint force expression in terms of frame $\{o\}$ is

$$\$^r = (\,1 \quad 0 \quad 0 \quad ; \quad 0 \quad -z \quad y\,) \tag{7}$$

where $(\,0 \quad y \quad z\,)^T$ is the central point vector of spherical joint with respect to frame $\{o\}$.

Equation (7) shows that the constraint force of RPS actuated branch is a space vector which passes through central point of spherical joint (S) and parallel to axis of revolute joint (R). Similarly, for SPR actuated branch, the constraint force expression in terms of frame $\{o\}$ is

$$\$^r = (\,l \quad m \quad n \quad ; \quad 0 \quad 0 \quad 0\,) \tag{8}$$

where $(\,l \quad m \quad n\,)^T$ is the direction vector of revolute joint (R). Since $(\,x \quad y \quad z\,)^T$ is the central point vector of revolute joint (R), the relationship, $lx + my + nz = 0$, holds.

Equation (8) shows that the constraint force of SPR actuated branch is a space vector which passes through central point of spherical joint (S) and parallel to axis of revolute joint (R). Combining with equations (7), (8), and type synthesis principle of vehicle-based stabilized platform, the type of PM is 2SPR/RPS, as shown in Figure 7. The typical structural forms of first and third actuated branches are SPR, the second actuated branch is RPS, and the constraint forces of each actuated branches are $\$_1^r$, $\$_2^r$, and $\$_3^r$, accordingly. The connection points between actuated branches and moving platform are a_1, a_2, and a_3, and the connection points between actuated branches and fixed platform are b_1,b_2, and b_3. Meanwhile, all revolute joint axes are parallel to x-axis; the translation joints can be realized by servo electric cylinder.

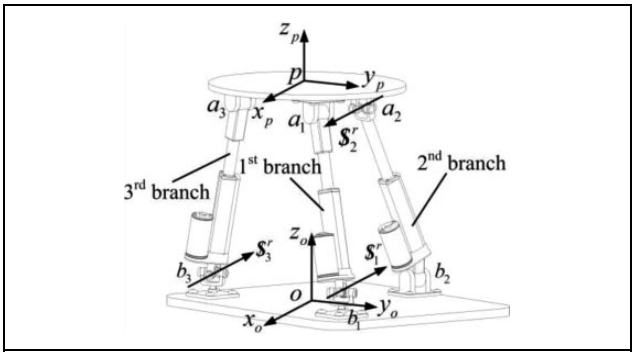


Figure 7. The 2SPR/RPS parallel mechanism.

Coupling kinematics analysis of parallel vehicle-based stabilized platform

Motion characteristic

Combining with equations (7) and (8), the constraint screws of moving platform in terms of frame $\{o\}$ can be described as

$$\begin{cases} \$_1^r = (\,1 \quad 0 \quad 0 \quad ; \quad 0 \quad 0 \quad m\,) \\ \$_2^r = (\,1 \quad 0 \quad 0 \quad ; \quad 0 \quad 0 \quad -m\,) \\ \$_3^r = (\,1 \quad 0 \quad 0 \quad ; \quad 0 \quad -n \quad 0\,) \end{cases} \tag{9}$$

where $m = |ob_1| = |ob_3|$ and $n = |ob_2|$.

Equation (9) shows that the constraint screws of moving platform are linear independence with each other. Hence, the independent DOFs of mechanism are three. Based on the concept of mathematics criterion of rigid-body continuous rotation axis, the continuous rotation axis is a space straight line which is parallel to constraint force vector or intersect on constraint point, and the movement tracking information is a space straight line which perpendicular to all constraint force vector. The constraint force vector of 2SPR/RPS, $\$_1^r$, $\$_2^r$, and $\$_3^r$ are all parallel to x_o-axis and satisfy the condition of non-coplanar. Above all, the continuous rotation axis of moving platform is x_o-axis, and the translation tracking is y_o- and z_o-axes.

The similar kinematics characteristic can be obtained by using above analysis method when the 2SPR/RPS PM at any poses in workspace. Over all, the vehicle-based stabilized platform based on the 2SPR/RPS PM can isolate external perturbation such as sway, heave, and roll, which

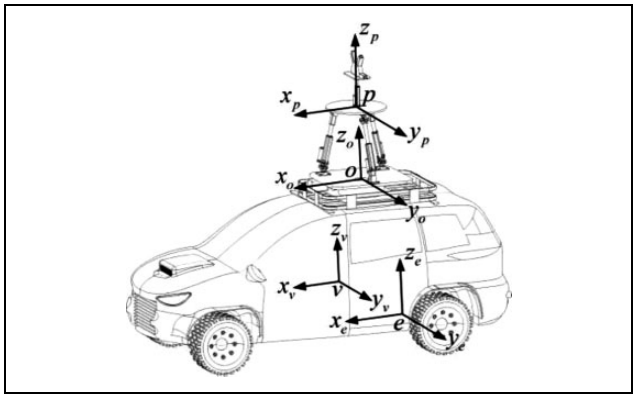


Figure 8. The coordinate system of vehicle-based stabilized platform.

can provide a relatively stable work environment for visual system.

Motion adjoint transformation

For the convenience of the reader, a sketch of stabilized platform frames is given in Figure 8; the frames can be described as follows.

(1) Inertial frame $\{e\}$: the origin is coincident with the center of vehicle, x_e-axis points to the direction of vehicle running, and z_e-axis is vertical up. (2) Vehicle frame $\{v\}$: the origin is coincident with the center of vehicle; the axes are parallel to frame $\{e\}$ when vehicle is in balance. (3) Fixed platform frame $\{o\}$: the origin is on the center of fixed platform, x_o-axis points to the running direction, y_o-axis points to tunnel surface, and z_o-axis is vertical up. (4) Moving platform frame $\{p\}$: the origin is on the center of moving platform, in which axes are parallel to the corresponding axis of frame $\{o\}$ when the mechanism is in initial posture.

The configuration matrix of moving platform with respect to frame $\{o\}$ is

$$\boldsymbol{g}_{op} = \begin{bmatrix} \boldsymbol{R}_{op} & p^o_{op} \\ \boldsymbol{0} & \boldsymbol{1} \end{bmatrix} = \boldsymbol{g}_{vo}^{-1}\boldsymbol{g}_{ev}^{-1}\boldsymbol{g}_{ep} \tag{10}$$

where $\boldsymbol{g}_{ep}$ is the configuration matrix of moving platform with respect to frame $\{e\}$; $\boldsymbol{g}_{ev}$ and $\boldsymbol{g}_{vo}$ are the configuration matrices of vehicle and moving platform with respect to frames $\{e\}$ and $\{v\}$, respectively.

Based on the multi-rigid-body acceleration adjoint transformation, the rigid-body velocity and acceleration of moving platform relative to frame $\{o\}$ in terms of frame $\{e\}$ can be described as

$$\begin{cases} \boldsymbol{V}^e_{op} = \boldsymbol{V}^e_{ep} - \boldsymbol{V}^e_{ev} - \boldsymbol{V}^e_{vo} \\ \hat{\boldsymbol{A}}^e_{op} = \\ \hat{\boldsymbol{A}}^e_{ep} - \{\hat{\boldsymbol{A}}^e_{ev} + \hat{\boldsymbol{A}}^e_{vo} + [\hat{\boldsymbol{V}}^e_{ev}, \hat{\boldsymbol{V}}^e_{vo}] + [\hat{\boldsymbol{V}}^e_{ev}, \hat{\boldsymbol{V}}^e_{op}] + [\hat{\boldsymbol{V}}^e_{vo}, \hat{\boldsymbol{V}}^e_{op}]\} \end{cases}$$

where $(\boldsymbol{V}^e_{ep}, \boldsymbol{A}^e_{ep})$ and $(\boldsymbol{V}^e_{ev}, \boldsymbol{A}^e_{ev})$ are rigid-body velocity and acceleration of moving platform and vehicle with respect to frame $\{e\}$, respectively. Since fixed platform is mounted to vehicle, the relationship, $\boldsymbol{V}^e_{vo} = \boldsymbol{A}^e_{vo} = \boldsymbol{0}$, holds. Therefore, the above equation can be sorted as

$$\begin{cases} \boldsymbol{V}^e_{op} = \boldsymbol{V}^e_{ep} - \boldsymbol{V}^e_{ev}, \\ \hat{\boldsymbol{A}}^e_{op} = \hat{\boldsymbol{A}}^e_{ep} - \hat{\boldsymbol{A}}^e_{ev} - [\hat{\boldsymbol{V}}^e_{ev}, \hat{\boldsymbol{V}}^e_{op}] \end{cases} \tag{11}$$

Furthermore, the configuration matrix of non-inertial frame $\{o\}$ relative to inertial frame $\{e\}$ is $\boldsymbol{g}_{eo} = \boldsymbol{g}_{ev}\boldsymbol{g}_{vo}$; the screws in equation (11) can be represented in terms of frame $\{o\}$ as

$$\hat{\boldsymbol{V}}^o_{op} = \boldsymbol{g}_{eo}^{-1}\hat{\boldsymbol{V}}^e_{op}\boldsymbol{g}_{eo}, \ \hat{\boldsymbol{A}}^o_{op} = \boldsymbol{g}_{eo}^{-1}\hat{\boldsymbol{A}}^e_{op}\boldsymbol{g}_{eo} \tag{12}$$

Substituting equation (11) into equation (12), the velocity adjoint transformation of moving platform and stabilized platform is given as

$$\boldsymbol{V}^o_{op} = \boldsymbol{Ad}^v_{\boldsymbol{g}_{op}}\boldsymbol{V}^e_{ep} + \boldsymbol{Ad}^v_{\boldsymbol{g}_{ov}}\boldsymbol{V}^e_{ev} \tag{13}$$

where $\boldsymbol{Ad}^v_{\boldsymbol{g}_{op}} = \begin{bmatrix} \boldsymbol{R}^{-1}_{eo} & 0 \\ -\boldsymbol{R}^{-1}_{eo}\hat{p}^e_{eo} & \boldsymbol{R}^{-1}_{eo} \end{bmatrix}$ and $\boldsymbol{Ad}^v_{\boldsymbol{g}_{ov}} = -\begin{bmatrix} \boldsymbol{R}^{-1}_{eo} & 0 \\ -\boldsymbol{R}^{-1}_{eo}\hat{p}^e_{eo} & \boldsymbol{R}^{-1}_{eo} \end{bmatrix}$.

Similarly, the acceleration adjoint transformation of moving platform and stabilized platform can be given as

$$\boldsymbol{A}^o_{op} = \boldsymbol{Ad}^v_{\boldsymbol{g}_{op}}\boldsymbol{A}^e_{ep} + \boldsymbol{Ad}^v_{\boldsymbol{g}_{ov}}\boldsymbol{A}^e_{ev} + (\boldsymbol{V}^e_{ev})^T\boldsymbol{Ad}^a_{\boldsymbol{g}_{vp}}\boldsymbol{V}^e_{ep} \tag{14}$$

where

$$\boldsymbol{Ad}^a_{\boldsymbol{g}_{vp}} = \begin{bmatrix} [-\boldsymbol{R}_{eo} * \boldsymbol{\Theta} \quad \boldsymbol{0}]^T & \boldsymbol{0} \\ [((\hat{p}^e_{eo})^{-1}\boldsymbol{R}_{eo}) * \boldsymbol{\Theta} - \boldsymbol{R}_{eo} * \boldsymbol{\Theta}]^T & [-\boldsymbol{R}_{eo} * \boldsymbol{\Theta} \quad \boldsymbol{0}]^T \end{bmatrix}_{6\times6\times6},$$

in which $\boldsymbol{\Theta} = \begin{bmatrix} 0 & -k & j \\ k & 0 & -i \\ -j & i & 0 \end{bmatrix}$; the element of this matrix is column vectors, that is, $\boldsymbol{i} = [1 \quad 0 \quad 0]^T$, $\boldsymbol{j} = [0 \quad 1 \quad 0]^T$, and $\boldsymbol{k} = [0 \quad 0 \quad 1]^T$.

Motion input-output mapping

Let $\boldsymbol{m}^p_i$ and $\boldsymbol{n}^o_i$ denote the position vector of hinge points of moving platform and fixed platform, respectively. Combining with equation (10), the posture input–output mapping of parallel vehicle-based stabilized platform can be established as

$$\bar{\boldsymbol{q}} = \boldsymbol{g}_{vo}^{-1}\boldsymbol{g}_{ev}^{-1}\boldsymbol{g}_{ep}\boldsymbol{m}^p_i - \boldsymbol{n}^o_i \tag{15}$$

According to the screw theory, the motion joint screw of actuated branch in terms of frame $\{o\}$ can be described as $\$^i_j$, in which i is the sequence number of actuated branch, and j is the sequence number of motion joint. The

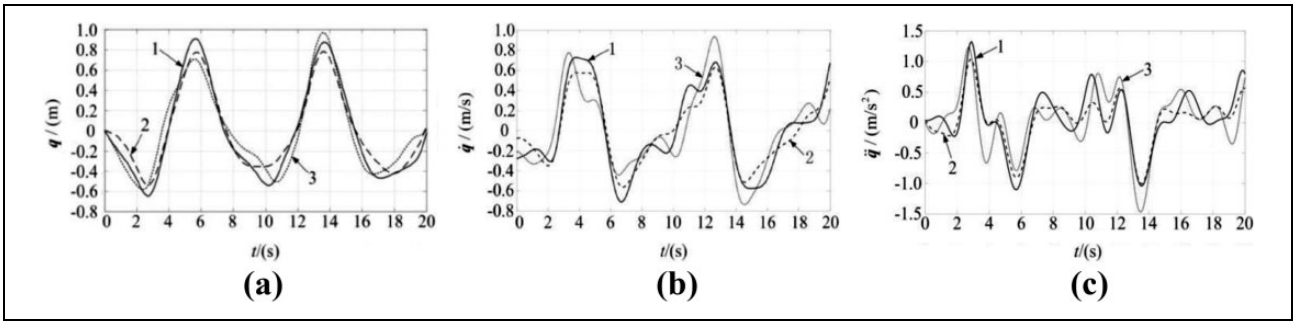


Figure 9. The calculation results of actuated branches. (a) Displacement, (b) velocity, and (c) acceleration.

relationship of velocity and acceleration between moving platform and actuated joints is

$$\begin{cases} \boldsymbol{V}_{op}{}^{0} = \varphi_1^i \$_1^i + \ldots + \varphi_5^i \$_5^i = G_\varphi^i \varphi^i \\ \boldsymbol{A}_{op}^0 = G_\varphi^i \varphi^i + (\varphi^i)^T H_\varphi{}^i \varphi^i \end{cases}$$

where $\boldsymbol{G}_{\varphi}^{i}$ is the Jacobian of the ith actuated branch and $[\boldsymbol{H}_{\varphi}^{i}]_{m,n}$ is the Lie brackets Jacobian of the ith actuated branch, in which $\boldsymbol{H}_{\varphi}^{\mathrm{H}}$ is given as

$$[H_\varphi{}^H]_{m,n}^{(i)} = \begin{cases} [\$_m^{(i)}, \$_n^{(i)}] & m < n \\ 0 & m - n \end{cases}$$

Extracting corresponding parts of the above equation, the velocity and acceleration mapping of moving platform to actuated branches can be established as

$$\boldsymbol{V}_{op}^{o} = \boldsymbol{G}\,\dot{\boldsymbol{q}},\ \boldsymbol{A}_{op}^{o} = \boldsymbol{G}\,\ddot{\boldsymbol{q}} + \dot{\boldsymbol{q}}^T \boldsymbol{H}\,\dot{\boldsymbol{q}} \tag{16}$$

where $\boldsymbol{G}$ and $\boldsymbol{H}$ are the Jacobian and Lie brackets Jacobian of velocity and acceleration of moving platform to input movements of actuated branches, respectively.

Combining with equations (13) and (16), the velocity input–output mapping of vehicle-based stabilized platform can be established as

$$\dot{\boldsymbol{q}} = \boldsymbol{J}_p \boldsymbol{V}_{ep}^{e} + \boldsymbol{J}_v \boldsymbol{V}_{ev}^{e} \tag{17}$$

where $\boldsymbol{J}_p = \boldsymbol{G}^{-1} \boldsymbol{Ad}_{\boldsymbol{g}_{op}}^{v}$ and $\boldsymbol{J}_v = \boldsymbol{G}^{-1} \boldsymbol{Ad}_{\boldsymbol{g}_{ov}}^{v}$.

Combining with equations (14) and (16), the input acceleration expression of actuated branches is

$$\ddot{\boldsymbol{q}} = \boldsymbol{J}_p \boldsymbol{A}_{ep}^{e} + \boldsymbol{J}_v \boldsymbol{A}_{ev}^{e} + (\boldsymbol{V}_{ev}^{e})^T \boldsymbol{h}_{vp} \boldsymbol{V}_{ep}^{e} - \dot{\boldsymbol{q}}^T \boldsymbol{h}_{\boldsymbol{q}} \dot{\boldsymbol{q}}$$

where $\boldsymbol{h}_{sp} = \boldsymbol{G}^{-1} * \boldsymbol{Ad}_{\boldsymbol{g}_{vp}}^{a}$ and $\boldsymbol{h}_{\boldsymbol{q}} = \boldsymbol{G}^{-1} * \boldsymbol{H}$.

By further simplifying and rearranging the above equations, the acceleration input–output mapping of vehicle-based stabilized platform can be established as

$$\begin{aligned} \ddot{\boldsymbol{q}} = {} & \boldsymbol{J}_p \boldsymbol{A}_{ep}^{e} + \boldsymbol{J}_v \boldsymbol{A}_{ev}^{e} + (\boldsymbol{V}_{ep}^{e})^T \boldsymbol{H}_{pp} \boldsymbol{V}_{ep}^{e} \\ & + (\boldsymbol{V}_{ev}^{e})^T \boldsymbol{H}_{vv} \boldsymbol{V}_{ev}^{e} + (\boldsymbol{V}_{ev}^{e})^T \boldsymbol{H}_{vp} \boldsymbol{V}_{ep}^{e} \end{aligned} \tag{18}$$

where $\boldsymbol{H}_{pp} = -\boldsymbol{J}_p^T \boldsymbol{h}_{\boldsymbol{q}} \boldsymbol{J}_p$, $\boldsymbol{H}_{vv} = -\boldsymbol{J}_v^T \boldsymbol{h}_{\boldsymbol{q}} \boldsymbol{J}_v$, and $\boldsymbol{H}_{vp} = \boldsymbol{h}_{vp} - \boldsymbol{J}_v^T \boldsymbol{h}_{\boldsymbol{q}} \boldsymbol{J}_p - (\boldsymbol{J}_p^T \boldsymbol{h}_{\boldsymbol{q}} \boldsymbol{J}_v)^T$.

Semi-physical simulation of parallel vehicle-based stabilized platform

System parameters

Taking the developed tunnel detection system as research object, the 2SPR/RPS PM has the dimensions of moving platform $d_1 = 1600$ mm, fixed platform $d_2 = 1800$ mm, and initial height $h = 1200$ mm.

For simplicity, the inertial movement of vehicle can be simulated using sine wave superposition. Hence, the motion laws of sway, heave, and roll can be given as

$$\begin{cases} \theta_x(t) = A_{R_x}^v \sin(2\pi t / T_{R_x}^v) \\ P_y(t) = A_{S_y}^v \sin(2\pi t / T_{S_y}^v) \\ P_z(t) = A_{S_z}^v \sin(2\pi t / T_{S_z}^v) \end{cases}$$

where $A_{R_x}^v = 5^\circ$; $A_{S_y}^v = 500\,mm$; $A_{S_z}^v = 500\,mm$; and $T_{R_x}^v = 3.1\,s$, $T_{S_y}^v = 4.9\,s$, and $T_{S_z}^v = 7.9\,s$ are amplitudes and periods of the above motion laws, respectively.

For kinematics analyzing of parallel vehicle-based stabilized platform, the motion laws of moving platform can be assumed as sinusoidal waveform. In view of the demands of digital camera for environment-stability performance, the amplitudes and periods of moving platform with respect to inertial frame are $A_{R_x}^p = 1^\circ$, $A_{S_y}^p = 10\,mm$, $A_{S_z}^p = 10\,mm$ and $T_{R_x}^p = 5.9\,s$, $T_{S_y}^p = 3.14\,s$, $T_{S_z}^p = 4.2\,s$, respectively.

System simulation

Based on the motion adjoint transformation and input–output mapping of vehicle-based stabilized platform, a theoretic calculation of displacement, velocity, and acceleration of actuated branches is given in Figure 9. Note that the main source of stabilized platform is vehicle's perturbation; the curves of each actuated branches are nearly the same; and the angle, velocity, and moment of motor will be peaked at the same time. From the graphs, it can be seen that the maximum input displacement, velocity, and acceleration of actuated branches are 0.85 m, 0.95 m/s, and 1.5 m/s^2, respectively.

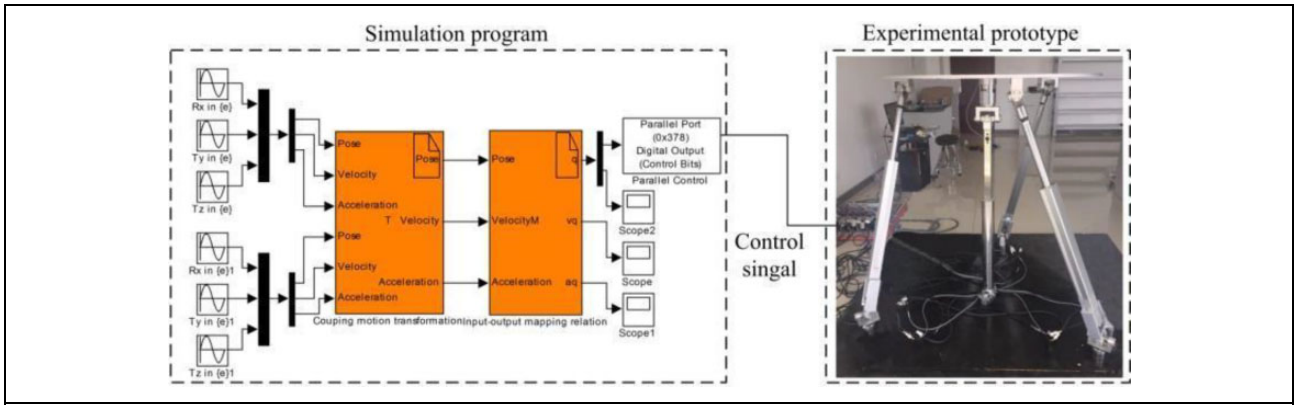


Figure 10. The semi-physical simulation model.

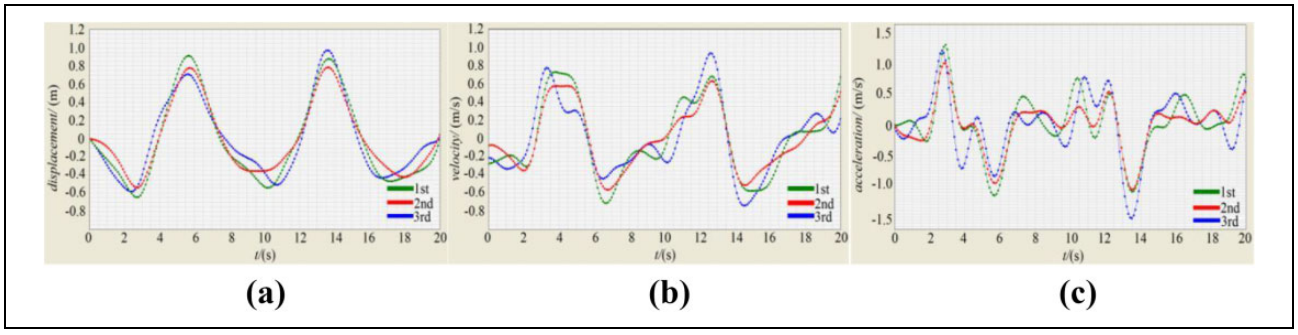


Figure 11. The simulation results of actuated branches. (a) Displacement, (b) velocity, and (c) acceleration.

Based on the obtained results from this article, our team developed a set of 2SPR/RPS PM prototype. Meanwhile, the vehicle-based stabilized platform is a multi-rigid-body system in non-inertial system, but the prototype is in inertial system. In order to verify the correctness of the theoretical analysis presented in this article, a semi-physical simulation model is built in Figure 10, which consists of simulation program and experimental prototype. The role of simulation program is to provide simulation signal for external perturbation of vehicle and movement of moving platform. Then the displacement, velocity, and acceleration of moving platform relative to inertial system can be obtained by equations (10), (13), and (14), respectively, and the displacement, velocity, and acceleration can be further calculated by equations (15), (17), and (18), respectively. Meanwhile, a detection branch is installed among actuated branches to obtain posture of moving platform.

On this basis, experimental prototype can be moved by control signal; the corresponding motion curves of each actuated branch can be given by TRIO controller, as shown in Figure 11. From the graphs, it can be seen that the simulation curves of displacement, velocity, and acceleration are fully consistent with theoretic calculation, which shows the high accuracy and efficiency of kinematics modeling method presented in this article.

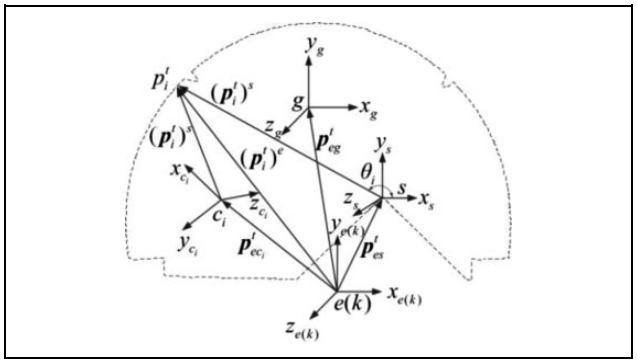


Figure 12. The diagram of coordinate system.

External parameters identity and analysis of vision system

Coupling posture identity and analysis of digital camera

A sketch of vision system frame is given in Figure 12. The frames can be described as follows: (1) inertial frame $\{e\}$: the origin is coincident with the install center k of multi-camera. x_e-axis is within the install plane of camera, horizontally pointing to tunnel surface; y_e-axis is vertical up; and z_e-axis points to the direction of vehicle running. (2) Installation frame $\{k\}$: x_k- and y_k-axes are within the install plane of cameras and along horizontal and vertical

direction, respectively; z_k-axis is perpendicular to the install plane of cameras. (3) Camera frame $\{c_i\}$: the origin is coincident with install center of multi-camera. x_{ci}-axis is perpendicular to the camera lenses, pointing to tunnel surface; y_{ci}- and z_{ci}-axes are parallel and perpendicular to the install plane of camera, respectively. (4) Scanner frame $\{s\}$ and INS frame $\{g\}$: the origin is located at the center of equipment. The axes are parallel to the corresponding axis of frame $\{k\}$.

When vehicle in quiescent state, the initial pose matrix and position vector of frame $\{c_i\}$, $\{s\}$, and $\{g\}$ with respect to frame $\{k\}$ and $\{e\}$ are $\boldsymbol{R}^0_{kc_i}$, $\boldsymbol{R}^0_{ks}$, $\boldsymbol{R}^0_{kg}$, $\boldsymbol{p}^0_{kc_i}$, $\boldsymbol{p}^0_{ks}$, and $\boldsymbol{p}^0_{kg}$, respectively.

Let $(\xi(t) \quad \psi(t) \quad \zeta(t) \quad x(t) \quad y(t) \quad z(t))$ is the pose parameters of moving platform at time t. $\boldsymbol{T}_{eg}(t) = \begin{bmatrix} \boldsymbol{R}_{eg}(t) & \boldsymbol{p}^e_{eg}(t) \\ \boldsymbol{0} & 1 \end{bmatrix}$ is the configuration matrix of INS in inertial frame $\{e\}$, in which $\boldsymbol{R}_{eg}(t) = \boldsymbol{R}(\boldsymbol{x}_g, \xi(t))\boldsymbol{R}(\boldsymbol{y}_g, \psi(t))\boldsymbol{R}(\boldsymbol{z}_g, \zeta(t))$ and $\boldsymbol{p}^e_{eg}(t) = [x(t) \quad y(t) \quad z(t)]^T$.

Based on the concept of multi-rigid-body transformation, the configuration matrix of digital camera with respect to frame $\{e\}$ can be given as

$$\boldsymbol{T}_{ec_i}(t) = \boldsymbol{T}_{eg}(t)\boldsymbol{T}_{gc_i}(t) \tag{19}$$

where $\boldsymbol{T}_{gc_i}$ is the configuration matrix of digital camera with respect to frame $\{g\}$. Since INS and digital camera are the same rigid-body, the configuration matrix between INS and digital camera is

$$\boldsymbol{T}_{gc_i}(t) = \boldsymbol{T}^0_{gc_i} = \boldsymbol{T}^0_{gk}\boldsymbol{T}^0_{kc_i} = (\boldsymbol{T}^0_{kg})^{-1}\boldsymbol{T}^0_{kc_i}$$

Combining with equation (19), the coupling pose of digital camera at any time can be established as

$$\boldsymbol{T}_{ec_i}(t) = \begin{bmatrix} R_{ec_i}(t) & p_{ec_i}(t) \\ 0 & 1 \end{bmatrix} = \boldsymbol{T}_{eg}(t)(\boldsymbol{T}^0_{kg})^{-1}\boldsymbol{T}^0_{kc_i} \tag{20}$$

The above equation establishes the digital camera coupling pose parameters disturbed by vehicle; the coupling rotation and translation are $R_{ec_i}(t)$ and $p_{ec_i}(t)$, respectively.

Object distance modeling and analysis of digital camera

In Figure 12, the dashed part is the sample curve of scanner at time t; the data format is $(d_j(t), \theta_j)$, in which $j = 1, \cdots, 1024$ and $\theta_j \in -135 - 135^\circ$. Let $p^t_j(t)$ denotes sample point of scanner on tunnel surface. Therefore, $d_j(t)$ is the distance between point s and $p_j(t)$. Then, θ_j is the sample angle.

The position vector of each sample point with respect to the scanner frame $\{s\}$ is $\boldsymbol{p}^s_j(t) = [d_j(t)\cos\theta_j \quad d_j(t)\sin\theta_j 0]^T$. According to the principle of space vector addition, the above position vector can be given in inertial frame $\{e\}$ as

$$\boldsymbol{p}^e_j(t) = \boldsymbol{R}_{es}(t)\boldsymbol{p}^s_j(t) + \boldsymbol{p}_{es}(t) \tag{21}$$

where $\boldsymbol{R}_{es}(t)$ and $\boldsymbol{p}_{es}(t)$ are the coupling rotation and translation of scanner at time t, respectively. The coupling pose of scanner can be given as

$$\boldsymbol{T}_{es}(t) = \begin{bmatrix} \boldsymbol{R}_{es}(t) & \boldsymbol{p}_{es}(t) \\ \boldsymbol{0} & 1 \end{bmatrix} = \boldsymbol{T}_{eg}(t)(\boldsymbol{T}^0_{kg})^{-1}\boldsymbol{T}^0_{ks} \tag{22}$$

Therefore, the position vector of each sample point $p_j(t)$ with respect to camera frame $\{c_i\}$ is written as

$$\boldsymbol{p}^{c_i}_j(t) = \boldsymbol{p}^e_j(t) - \boldsymbol{p}_{ec_i}(t)$$

where $\boldsymbol{p}^{c_i}_j(t)$ is the object distance vector expression of camera. Substituting equations (21) and (22) into above equation, the object distance expression between digital camera and tunnel surface at any moment can be simplified as

$$u(t) = |\boldsymbol{R}_{eg}(t)(\boldsymbol{R}^0_{kg})^{-1}(\boldsymbol{R}^0_{ks}(\boldsymbol{p}^s_j(t) + \boldsymbol{p}^0_{ks}) - \boldsymbol{R}^0_{kc_i}\boldsymbol{p}^0_{kc_i})| \tag{23}$$

Conclusion and future works

1. The sway, heave, and roll caused by external perturbation of vehicle severely affect vision system. Numerical calculation and field testing show the variation ranges are Tx: ± 0.6 m, Ty: ± 0.55 m, Rz: $\pm 0.5^\circ$. Based on this, a new type of 2SPR/RPS PM has been synthesized.
2. The motion adjoint transformation and input–output mapping between external perturbation and mechanism movement are built. In addition, an experimental prototype is developed, and the correctness of theoretical analysis is verified by semi-physical simulation.
3. On this basis, the mathematical expressions of coupling posture and object distances of visual system are proposed. It can provide evidence for digital image correcting and geometric measuring in next step.

In the near future, the control strategy of 2SPR/RPS PM prototype will be solved by kinematics mapping relationship, and the compensation ability evaluation index of stabilized platform will be studied. On this basis, we should focus on time-delay estimation method to realize high-accuracy stabilization for vehicle-based stabilized platform. Meanwhile, the image-processing systems of tunnel detection vehicle will be optimized by the mathematical expressions of coupling posture and object distances of visual system presented in this article, and the measuring modeling between disease geometry and object distance will be developed.

Acknowledgements

The authors sincerely thank to Professor Tieshi Zhao of Yanshan University for his critical discussion of PM type synthesis and Professor Qingyong Li of Beijing Jiaotong University for his critical discussion of machine vision.

Declaration of conflicting interests

The author(s) declared no potential conflicts of interest with respect to the research, authorship, and/or publication of this article.

Funding

The author(s) disclosed receipt of the following financial support for the research, authorship, and/or publication of this article: This work was supported by National Natural Science Foundation of China (grant no 51705229) and the National Natural Science Foundation of Shanxi Province (grant no 2017-1-25).

ORCID iD

Xiao Liu https://orcid.org/0000-0001-5430-4032

References

1. Wang R, Qi TY, Lei B, et al. Study on the characteristic extraction of tunnel lining cracks. *Chin J Mech Eng* 2015; 06: 1211–1217.
2. Yma HH, Hook JJ, Schmidit B, et al. Seismic design and analysis of underground structures. *Tunnel Undergr Space Technol* 2001; 16(4): 247–293.
3. Zakeri H, Nejad FM, and Fahimifar A. Image based techniques for crack detection, classification and quantification in asphalt pavement: a review. *Arch Comput Method Eng* 2016; 24(4):1–43.
4. Medina R, Llamas J, Gómez-García-Bermejo J, et al. Crack detection in concrete tunnels using a Gabor filter invariant to rotation. *Sensors* 2017; 17(7): 1670–1681.
5. Iwamoto T, Enaka T, and Tada K. Development of testing machine for tunnel inspection using multi-rotor UAV. *J Phys Conf Ser* 2017; 842(1): 110–125.
6. Cubero FA and Rodriguez LJ. Efficient pavement crack detection and classification. *Eurasip J Image Vide* 2017; 2017(1):39–50.
7. Loce RP, Bernal EA, and Wu W. Computer vision in roadway transportation systems: a survey. *J Electron Imaging* 2013; 22(22):451–459.
8. Yong Y W, Fu W, Deng Q L, et al. A comparative study of vision detection and numerical simulation for laser cladding of nickel-based alloy. *J Manuf Process* 2017; 28:100–118.
9. Liu X, Li Y, Xue C M, et al. Optimal modeling and parameter identification for visual system of the road tunnel detection vehicle. *Chinese Journal of Scientific Instrument* 2018; 5: 152–160.
10. Attard L, Debono CJ, Valentino G, et al. Vision-based change detection for inspection of tunnel liners. *Automat Constr* 2018; 91: 142–154.
11. Qian B, Tang ZM, Shen XB, et al. Pavement crack detection based on multi-feature manifold learning and matrix factorization. *Chine J Sci Instrum* 2016; 37(07): 1639–1646.
12. Yoshitake I, Maeda T, and Hieda M. Image analysis for the detection and quantification of concrete Bugholes in a tunnel lining. *Case Stud Construct Mater* 2018; 8: 116–130.
13. Ortner T, Sorger J, and Piringer H. Visual analytics and rendering for tunnel crack analysis. *Visual Comput* 2016; 32(6–8): 859–869.
14. Stent S, Gherardi R, and Stenger B. Visual change detection on tunnel linings. *Mach Vision Appl* 2016; 27(3): 319–330.
15. Xu T, Zhu Z, Guo Y, et al. Development of road surface inspection system based on computer vision with improved neural network. *J Wuhan Univ Technol* 2012; 36(01): 34–37.
16. Fang XY, Kan WR, and Cheng SW. Motion-modeling-oriented camera response function estimation method for motion blurred images. *J Comput Aided Design Comput Graph* 2015; (07): 1238–1246.
17. Zhou XY, Zhu J, and Zhao BL. Extended state observer/proportion integration differentiation compound control based on dynamic modelling for an aerial inertially stabilized platform. *Int J Adv Robot Syst* 2017; 14(6): 1–10.
18. Herbuś K and Ociepka P. Integration of the virtual model of a Stewart platform with the avatar of a vehicle in a virtual reality. *Mater Sci Eng Conf Ser* 2016; 145(4): 26–35.
19. Xiang DM, Gao F, and Wu SF. Type synthesis of parallel robotic mechanisms: framework and brief review. *Mech Mach Theory* 2014; 78: 120–138.
20. Slobodan T, Milan Z, and Ratko G. Program suite for conceptual designing of parallel mechanism-based robots and machine tools. *Int J Adv Robot Syst* 2013; 10(6): 279–292.
21. Masroor H, Shahab UA, and Tareq M. Performance analysis of parallel stabilized mixed Galerkin method for three-dimensional transient Darcy flow using mesh reordering techniques. *J Petrol Sci Eng* 2019; 21: 256–275.
22. Deira SM, Esther LG, and Manuel AM. ADAMS-MATLAB co-simulation for kinematics, dynamics, and control of the Stewart–Gough platform. *Int J Adv Robot Syst* 2017; 14(4): 1–10.
23. Hussein T and Ernesto RL. Instantaneous kinematics analysis via screw-theory of a novel 3-CRC parallel mechanism. *Int J Adv Robot Syst* 2016; 13(3): 128–144.
24. Louis TS and Clément G. Kinematically redundant planar parallel mechanisms: kinematics, workspace and trajectory planning. *Mech Mach Theory* 2018; (119): 91–105.
25. Stefan S and Shao ZF. Kinematic analysis of the X4 translational–rotational parallel robot. *Int J Adv Robot Syst* 2018; 15(5): 1–12.
26. Liu X, Zhao TS, and Gao JW. Dynamic modeling and analysis of ship-based stabilizing platform in non-inertial system. *Robotics* 2014; 36(04): 411–418.

27. Tang HY, Zhang D, and Guo S. Kinematics analysis of a novel 2R1T parallel mechanism. *Int J Robot Autom* 2018, 33(2): 120–132.
28. Wu J, Zhang BB, and Wang LP. A measure for evaluation of acceleration of redundant and non-redundant parallel manipulators. *J Mech Robot* 2016; 8(2): 8.
29. Liang L, Puhua T, and Bai C. Dynamical modeling and structural parameter optimization of a novel spiral in-pipe robot. *Int J Robot Autom* 2016; 31(1): 78–89.
30. Aspragathos NA and Dimitros JK. A comparative study of three methods for robot kinematics. *IEEE Trans Syst Man Cybern* 1998; 28(2): 135–145.
31. Hunt KH. *Kinematic geometry of mechanism*. Oxford: Oxford University Press, 1978.
32. Duffy J. *Statics and kinematics with applications to robotics*. Cambridge: Cambridge University Press, 1996.
33. Phillips J. *Freedom in machinery, Volume 1, Introducing screw theory*. Cambridge: Cambridge University Press, 1984.
34. Chen GL, Yu WD, and Chen C. A new approach for the identification of reciprocal screw systems and its application to the kinematics analysis of limited-DOF parallel manipulators. *Mech Mach Theory* 2017; 118: 194–218.
35. Zeng XH, Chen J, and Peng LK. Statics analysis of 6-DOF parallel robot based on screw theory. *Appl Mech Mater* 2014; 536 (72): 965–969.
36. Liu X. Design and implementation of road tunnel intelligent detection system. *Machinery Design & Manufacture* 2018; 8: 66–68.
37. Liu X, Luo EJ, and Lei J. A new method for acceleration analysis of multi-rigid-body systems and its application for parallel ship-based stabilized platform. *Int J Robot Autom* 2018; 33(03): 219–225.